Leveraging Flexibility in the Design of a Wave Energy Converter: Strongly Coupled Two-Way FSI Numerical Modeling and Experimental Wave Tank Testing

J. Andersen, F. Ferri & C. Eskilsson
Department of the Built Environment
Aalborg University, Aalborg, Denmark

S.G. Thomsen & M. Folley
Wavepiston A/S, Helsingør, Denmark

ABSTRACT: The influence from the flexibility of plates on the hydrodynamic loads of an oscillating wave surge converter (OWSC) is investigated. Rigid and flexible plate designs have been tested with both numerical and experimental (physical wave tank) modeling. A strongly coupled two-way fluid-structure interaction (FSI) numerical model with scale-resolving CFD is benchmarked against experimental results and high compliance is observed. Promising results are found on how flexibility can be leveraged in the design of an OWSC to reduce extreme loads while maintaining operational loads. Further analyses and tests are pending.

1 INTRODUCTION

Wavepiston A/S is a Danish wave energy converter (WEC) company that has developed an oscillating wave surge converter (OWSC) type WEC with wave-activated bodies in the form of plates placed on a string. The plates and substructure experience very large impact loads when the hydraulic piston (PTO) reaches end-stop and in general from extreme wave events, where also slamming loads are of concern. The purpose of the present paper is to investigate the feasibility of using a composite material for the plates to allow deformation of the plates under extreme loading, see Figure 1, which yields significant load reductions, while maintaining high-capacity factors in the operational sea states.

Figure 1: Conceptual illustration of the storm protection mechanism of the Wavepiston sail.

1.1 *Plates in nominally normal flow*

The force on rigid flat plates in a nominally normal steady flow is governed by the shedding of large vortices (of similar size to the characteristic length of the plate) for practical Reynolds numbers $R_e > 10^3$ (Hoerner 1965). For sharp-edged plates with thickness-to-characteristic-length ratios less than 5%, the drag will virtually be equal to the pressure drag and the separation points are fixed at the plate edges, yielding a very weak R_e dependency in said range (Nakaguchi et al. 1968, Hoerner 1965). In the case of small-amplitude oscillatory flows – corresponding to Keulegan-Carpenter numbers $K_C \leq 0.15$ (Tian et al. 2016) – the force is inertia dominated and can be accurately calculated by potential flow theory as, e.g., seen in DNV (2017). For finite amplitude oscillatory flows $K_C > 0.15$ with velocities of $R_e > 10^3$, turbulent effects become substantial and both inertia and drag coefficients are strongly K_C dependent but remain only weakly dependent on the oscillation frequency and thus R_e (Lake et al. 2000, Tian et al. 2016). Introducing a free surface to the oscillatory flow of flat plates will allow for wave radiation and wave diffraction which will greatly impact the flow and make the force coefficients dependent on the oscillation frequency. The combined effects of geometrically dependent shed vortices and a free surface make the prediction of forces on flat plates in a nominally normal

oscillatory flow in the vicinity of a free surface complicated and calls for the use of high-fidelity Computational Fluid Dynamics (CFD) models.

1.2 *The Wavepiston wave energy converter*

The Wavepiston OWSC consists of multiple floating modules, called Energy Collectors (ECs), comprising wave-activated bodies in the form of surging plates (or paddles), support structures (EC beam and wagon), telescopic hydraulic pumps, and more, as illustrated in Figure 2. The multiple surging plates installed on each EC are collectively referred to as a *sail*. As ocean waves excite the sails, these will move relative to the EC beam which actuates the hydraulic pumps. Pressurized seawater is then pumped to shore to drive a turbine or desalination plant. The ECs are installed on a shared string reducing the total loads on the OWSC and thus mooring loads as well as smoothing the power curve. Currently, the Wavepiston OWSC is undergoing full-scale sea trials at the PLOCAN test site off the coast of the Canary Islands.

The added mass of a rectangular rigid plate in a nominally normal oscillatory flow (and without boundary effects) scales with its characteristic length cubed under potential flow assumptions (DNV 2017). Using the outer dimensions of 4 m $\times$ 8 m of the surging plates of the Wavepiston demonstrator deployed at PLOCAN this corresponds to an added mass of 78 tons on each EC. In operational sea states, the wave excitation force of the OWSC is inertia dominated, and a high added mass is thus favorable to maximize the capacity factor. However, in extreme sea states, the surging plates will reach the ends of the EC beam, which will result in rapid decelerations of the plate and its significant added mass, leading to very high structural requirements to the EC. To mitigate such hard end-stop forces and ultimately reduce the Levelized Cost of Energy (LCoE) of the OWSC, the implementation of a storm protection mechanism is crucial. For this purpose, each EC of the demonstrator at PLOCAN was constructed with multiple plates that mechanically rotate in yaw when approaching the end-stop, see Figure 2. This effectively reduced extreme loads, but the many components and rotating mechanisms in the harsh marine climate made the design unfeasible.

To avoid the rotating plates a new design is tested. It employs polymer composites for the sails to allow for large bending in extreme sea states as shown in Figure 1.

1.3 *Scope of the paper*

The flow and structural response of the hydro-elastic problem of flexible plates undergoing large deformations from hydrodynamic loads are highly interdepedent and the problem falls under the category

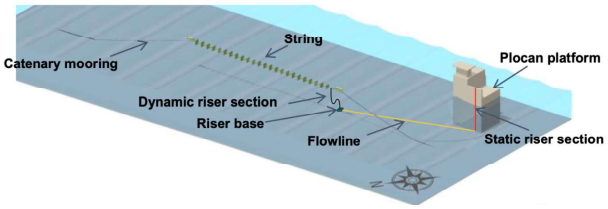

(a)

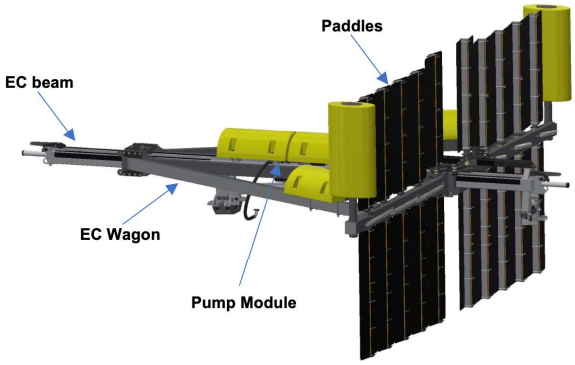

(b)

Figure 2: Wavepiston OWSC: (a) overview of entire system and (b) zoom-in on the EC.

of strongly coupled two-way fluid-structure interaction (FSI). The scope of the present paper is to i) benchmark a strongly coupled two-way FSI numerical model against experimental wave tank tests for a test case involving large deformations of flexible plates in a nominally normal oscillatory flow near a free surface and ii) investigate how the flexibility of the surging plate affects the structural response in said test case based on both numerical modeling and experimental wave tank testing.

2 EXPERIMENTAL WAVE TANK TESTS

The results of the numerical model are compared to the experimental data set generated in two distinct test campaigns. The first test campaign focused on the load measurement of full and slotted rigid sails, while the second campaign focused on sails made of flexible plates. The flexible plates were of PVC with thicknesses d_t of 0.3, 0.4, and 0.5 mm. With case 0.4 mm representing the baseline the other two represent about 50% and 200% bending stiffness variations. The tests were carried out in the wave basin at the Ocean and Coastal Engineering Laboratory of Aalborg University, Denmark. The basin measures 14.6 m $\times$ 19.3 m $\times$ 1.5 m (length $\times$ width $\times$ wall height) with an active test area of 8.4 m $\times$ 13.0 m (length $\times$ width). The basin is equipped with a snake-type wave generation system composed of 30 linked pistons. The experimental model is a 1:16 scaled version of the current design, comprising:

- Linear Actuator (LA): LinMot EM01-48-1250
- Sail (MP)
- Sail support structure (PS)

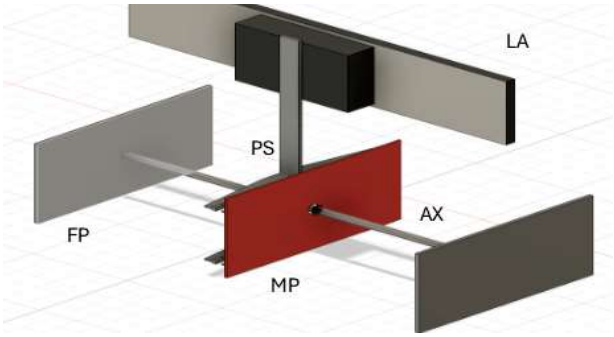

Figure 3: CAD model of the experimental setup.

- Load cells (LC): FUTEK S-Beam LSB210
- SCADA system

The 3D drawing of the experimental model is presented in Figure 3 along with the detailed view of the sail support structure. The version of the experimental model included a central axle (AX) and two static end plates (FP). These elements were removed in the tests investigated in the present paper to focus on the hydrodynamics of the sail. The SCADA system consisted of the LinMot Motor driver, SpeedGoat Real-Time Computer, the IO135 DAQ Input Output Module, and the host computer; further details can be found in (Ringwood et al. 2019). Photos of the experimental setup in the wave tank can be seen in Figure 4.

2.1 *Test program*

Both experimental campaigns (i.e., with rigid and flexible sails) included test programs with a combination of radiation and excitation tests. Radiation tests were carried out with regular (monochromatic) signals, irregular (chirp) signals, and impulse-like signals with very large decelerations (top-hat inspired). Due to brevity and given the significant computational overhead of the two-way FSI numerical model, this paper will focus on two selected regular radiation test conditions; RW04 (low amplitude) and RW06 (high amplitude). The conditions are detailed in Table 1. Abbreviations K1-3 refer to the flexible sails with K1 denoting the lowest bending stiffness and K3 the highest. The relative submergence is defined as

Figure 4: Experimental setup with flexible sail.

Table 1: Test conditions RW04 and RW06 as well as flexible sail dimensions, see Figure 5. *Definitions as per Tian et al. (2016).

Parameter	Value
Amplitude a {RW04, RW06}	{23, 78} mm
Period T	2.25 s
Submergence s	0.22 m
Water depth d	1.00 m
K_C * {RW04, RW06}	{0.36, 1.23}
R_e * {RW04, RW06}	$\{2.6, 8.7\} \cdot 10^4$
Relative submergence s_r	0.88
Sail width d_w	500 mm
Sail height d_h	250 mm
Plate height d_{hp}	202 mm
Flexible plate width d_{wp}	60.8 mm
Rigid plate width (inner) d_{wi}	10.0 mm
Rigid plate width (outer) d_{wo}	56.1 mm
Plate spacing d_{sp}	1 mm
Plate thickness d_t {K1, K2, K3}	{0.3, 0.4, 0.5} mm

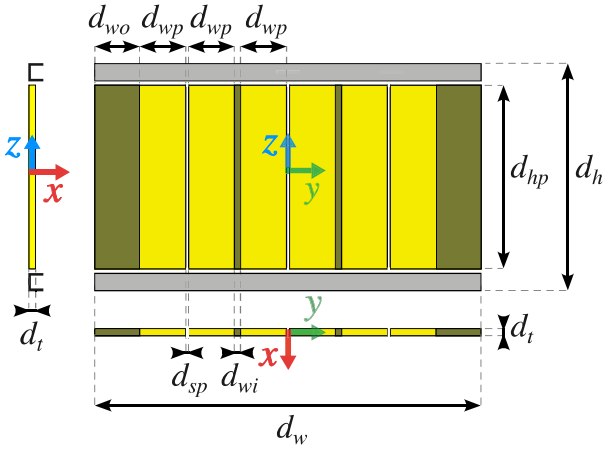

Figure 5: Simplified geometry of the flexible sail from the wave tank tests. Flexible plate parts are shown in yellow.

$s_r = s/d_h$. The regular radiation signals had a duration of $6T$ including a sinusoidal ramp-up over $2T$. The flexible sails consisted of four plate sections attached to supporting aluminum beams that connected the sail to the four load cells. The gaps between the free ends of the flexible plates measured $d_{sp} = 1$ mm. A simplified representation of the flexible sail is shown in Figure 5 with dimensions given in Table 1. The rigid sail (R) tested in the first campaign had the same outer dimensions $d_h \times d_w$ as the flexible sails (K1-3). Young's modulus and the density of the flexible plates were estimated to 2.55 GPa and 1458 kg/m^3 from dedicated tests. The former is based on linear Bernoulli-Euler beam theory with small loads and displacements measured on beams cut of the PVC materials.

3 NUMERICAL MODEL

The numerical models of the present study were set up using the commercial multi-physics framework of Simcenter Star-CCM+ v2406 (SDIS 2024) facilitating an integrated partitioned approach to the FSI problem. This allowed a socket-based (rather than file-based) data exchange, which is highly computationally advantageous for the implicit surface coupling required for strongly coupled two-way FSI. Finite vol-

ume and finite element discretization methods were utilized for the CFD and computational solid dynamics (CSD), respectively.

3.1 *Fluid partition*

A segregated flow solver with a transient implicit time model and the SIMPLE algorithm for pressure-velocity coupling was employed for the CFD. The free surface was modeled from the Volume-of-Fluid (VoF) method with the High-Resolution Interface Capturing (HRIC) convection scheme algorithm (SDIS 2024). In Andersen & Eskilsson (2023), a scale-resolving hybrid URANS-LES method was succesfully applied to model the highly turbulent large-curvature flow of a flat rigid plate in a nominally normal flow. Based on this, a similar approach was adopted for the present study, namely the Scale-Resolving Hybrid (SRH) model with k-ω SST turbulent closure (Duffal et al. 2019, SDIS 2024).

Each of the four plate sections was meshed with individual overset meshes, see Figure 6, allowing for the large rigid body translations of the RW06 signal. The overset mesh morphed with the FSI interface, as shown in Figure 6(a), to minimize the distortion of overset cells due to plate deformations. The small gaps between the flexible plates were modeled from overlapping overset meshes, see Figure 6(b), where an overset hierarchy dictates which region is considered the overset and the background. The mesh resolution in the dominant overlapping overset region must be sufficiently small to resolve the plate geometry of the recessive ('background') region. However, with $d_t = 0.3$ mm for the most flexible sail, this means that several million overset cells were required to resolve the recessive plate geometry. To mitigate the already very substantial computational cost, an artificially large $d_t = 3$ mm was used for the present numerical model resulting in significantly reduced simulation times. The Young's modulus and density were changed to keep the bending stiffness EI and total mass of the plate constant. The two horizontal supporting beams from the experimental model (shown in grey in Figure 5) were not included in the numerical to reduce complexity. Instead, the height of the surging plates was changed to $d_{hp} = d_h$ in order to keep equal outer dimensions of the sail in the experimental and numerical model.

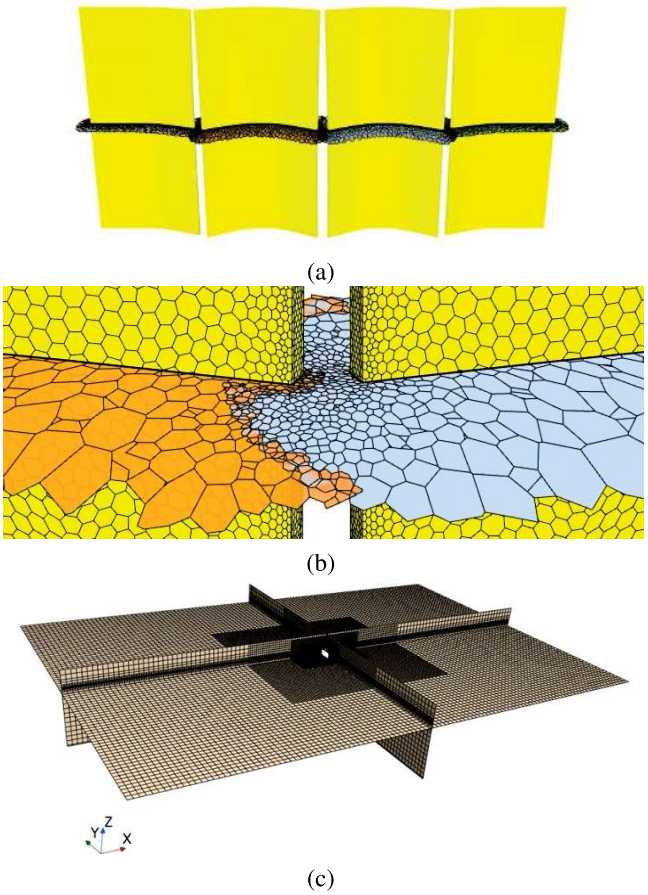

Figure 6: Fluid partition mesh: (a) the overset regions and FSI surface of the deformed flexible sail, (b) gap and overlapping overset regions, and (c) background region with refinement regions and AMR around the free surface.

Polyhedral cells with inflation layers were used for the overset meshes while hexahedral cells with refinement zones and automatic mesh refinement (AMR) around the free surface were used for the background mesh; see Figure 6(c). A no-slip boundary condition (BC) was imposed on the plate while relaxation zones with relaxation toward stagnant water were defined to all sides. A zero pressure BC was imposed for the top boundary, while a slip BC was used for the bed. The initial condition (IC) of the fluid partition was stagnant water.

3.2 *Solid partition*

The CSD adopted an isotropic linear elastic material law with the Green-Lagrange finite (nonlinear) strain measure. The stiffness matrix was updated at each iteration within each time step (full Newton method). At each iteration, the MUMPS sparse direct solver was used to solve the linearized set of equations. Time integration was carried out with the first-order backward Euler method.

The mesh consisted of HEX8 elements with bubble degrees of freedom to overcome locking. Fixed structure-structure interfaces were created between flexible and rigid plate parts (dark yellow in figure 5). Prescribed motion was imposed to the rigid plate parts. The IC of the solid partition was the undeformed sail subjected to hydrostatic loading.

3.3 *Surface coupling*

The fluid-structure interface was non-conformal with surface mapping from a nearest-neighbor interpolation stencil. Strongly coupled two-way FSI problems with structure-to-fluid density ratios of about one and incompressible fluids suffer from inherent artificial

added mass instabilities (Förster et al. 2007). To mitigate these instabilities, implicit surface coupling with a low displacement tolerance of minimum 10^{-4} mm or a maximum of 200 inner iterations was employed together with the Dynamics FSI stabilization scheme (SDIS 2024) and time-marching with a constant time step of 0.005 s.

The computational overhead of the RW06 simulations for the R and K1 sails is summarized in Table 2. No. of cores refers to physical CPU cores on a single CPU (AMD EPYC 7702, base clock speed 2.0 GHz).

Table 2: Computational overhead of the numerical models. Wall clock time is given for the simulation of $3T$ physical time.

Sail (FSI type)	R (one-way)	K1 (two-way)
Grid count	$4.5{\cdot}10^6$	$4.7{\cdot}10^6$
Wall clock time [h]	16	139
No. of cores	62	124

4 BENCHMARKING OF NUMERICAL TESTS AGAINST EXPERIMENTAL TESTS

To assess the accuracy of the numerical model, radiation tests with the RW06 signal (specified in Section 2) is used to benchmark the numerical model against the experimental tests. Comparison of the experimental and numerical force time series for both the rigid (R) and most flexible (K1) sails can be seen in Figures 7 and 8. The force time series were aligned by trigger signals from the experimental tests and subsequently imposing a corrective delay from maximizing the cross-correlation between the experimental and numerical position signals. The force time series were low-pass filtered (cut-off at 2 Hz) to remove noise and structural dynamic amplification from the experimental data. For consistency, the same filter was applied to the numerical and experimental data. The inertia force from accelerating the mass of the sails in the experimental tests was subtracted from the force time series. The full duration of $6T$ (including $2T$ ramp-up) of the experimental force time series is used in the comparison to the one-way FSI numerical model (rigid sail) in Figure 7. However, due to the very large computational overhead of the two-way FSI numerical model, only a duration of $3T$, i.e., one fully ramped period, is considered in Figure 8.

Very high agreement between the wave tank tests and the one-way FSI numerical model can be seen from the force time series in Figure 7. The force extremes maximally deviate with 3.0% (0.9 N) and the signals correlate very well with a Pearson correlation coefficient of 99.5% over the duration $6T$. In spite of the increased complexity and simplifying assumptions of the two-way FSI numerical model – including an artificially large thickness and the disregarding of the supporting horizontal beams, see Section 3 – high compliance between the numerical and experimental force time series is maintained as can be seen from Figure 8. Here, the maximum force peak deviation is 5.4% (1.1 N) and the Pearson correlation coefficient 99.9%.

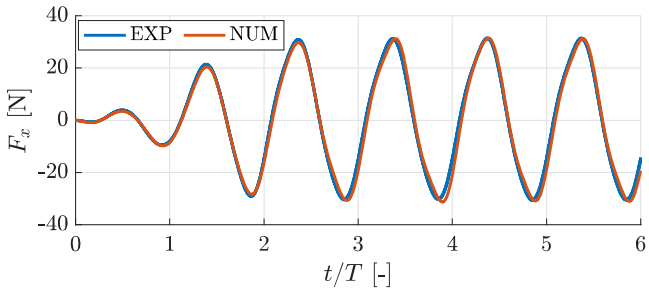

Figure 7: Benchmarking of force series for the R (rigid) sail.

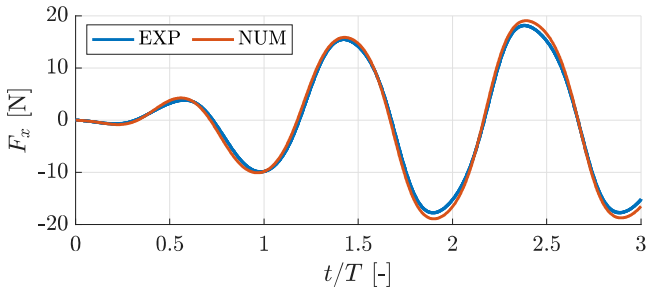

Figure 8: Benchmarking of force series for the K1 flexible sail.

5 THE EFFECT OF FLEXIBILITY

The influence of sail flexibility on the hydrodynamic loads in low and high amplitude conditions, RW04 and RW06, can be investigated from Figures 9(a) and 9(b) where the experimental force time series (five repetitions) for the R and K1-3 sails are compared. In the low amplitude condition, the force peaks from the flexible sails are not decreased relative to the rigid. Interestingly, in this condition, the largest force peaks are measured with the most flexible sail (K1). This is interpreted as a result of the changed natural frequency of the K1 sail from its added bending degrees of freedom. In the large amplitude condition, the force peaks of the K1 sail is substantially reduced relative to the more rigid sails. The reduction in the maximum absolute force peak between the R and K1 sail is 42.7%. Furthermore, the phase of the force time series for K1 has shifted, yielding increased correlation with the prescribed velocity (rather than acceleration) of the sail – underlining the significantly reduced added mass of the most flexible sail.

The two-way FSI numerical model shows findings similar to the experiments when comparing the force time series of the R and K1 sails. Comparing the dynamic surface pressure distributions of the R and K1 sails in their respective local force peaks at about $t = 2.9T$ reveals how areas of high pressure for the R sail are significantly reduced for the K1 sail, see Figure 10. Furthermore, the integrated projected pressure normal to the prescribed motion direction is reduced from the increased porosity and the changed surface normals due to large deformations.

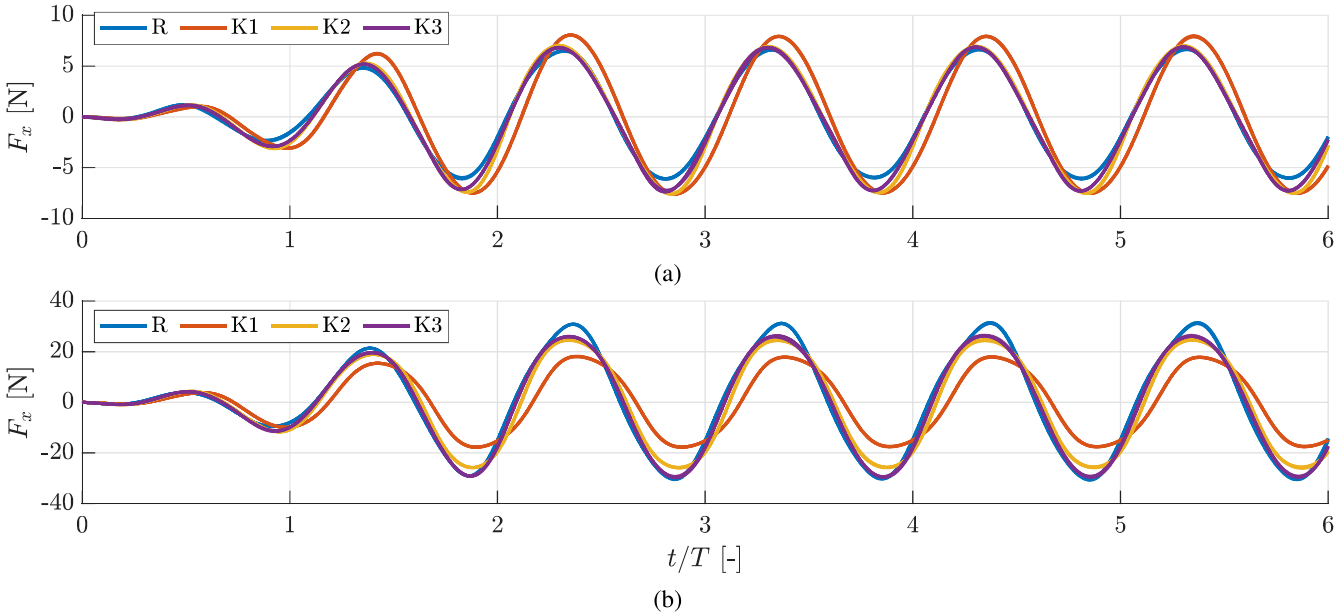

Figure 9: Force time series for varied flexibility of the sail under wave tank testing. Test conditions (a) RW04 and (b) RW06.

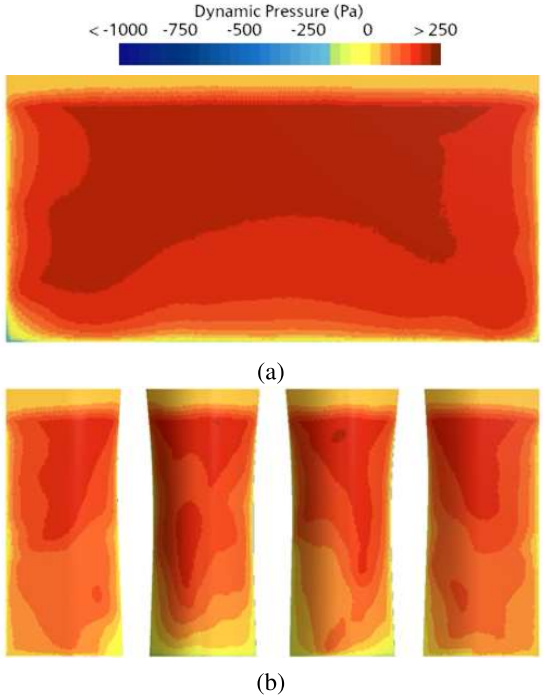

Figure 10: Pressure distributions of (a) the R sail and (b) the K1 sail at their respective local force peaks around $t = 2.9T$.

6 CONCLUSIONS AND FURTHER WORK

A strongly coupled two-way FSI numerical model simulating the nominally normal oscillatory flow of flexible plates in the vicinity of a free surface has been benchmarked against experimental wave tank tests showing high accuracy on force prediction. Experimental and numerical results show how flexible plates can be leveraged to reduce extreme loads while maintaining (or even slightly increasing) operational loads relative to rigid plates with the same outer dimensions. Implementing these effects into the design of an OWSC can yield an efficient and feasible storm protection without reducing the capacity factor. Further analyses and tests are pending including the numerical modeling of hard end-stops.

ACKNOWLEDGMENTS

This work was supported by the Danish Energy Technology Development and Demonstration Program (EUDP) through project no. 640231-510302.

REFERENCES

Andersen, J. & C. Eskilsson (2023). Detached-Eddy Simulation of Normal Flow past Flat Plates: The Influence from Corner Curvature. *Int. J. Offshore Polar Eng. 33*, 359–366.

DNV (2017). Environmental Conditions and Environmental Loads.

Duffal, V., B. Meux, & R. Manceau (2019). Development and Validation of a Hybrid RANS-LES Approach Based on Temporal Filtering. In *Proc. ASME-JSME-KSME 2019 8 Joint Fluids Eng. Conf. Vol. 2: Comp. Fluid Dyn.*

Förster, C., W. A. Wall, & E. Ramm (2007). Artificial Added Mass Instabilities in Sequential Staggered Coupling of Nonlinear Structures and Incompressible Viscous Flows. *Comput. Methods Appl. Mech. Eng. 196*(7), 1278–1293.

Hoerner, S. F. (1965). *Fluid-Dynamic Drag*. Published by the Author.

Lake, M., H. He, A. W. Troesch, M. Perlin, & K. P. Thiagarajan (2000). Hydrodynamic Coefficient Estimation for TLP and Spar Structures. *J. Offshore Mech. Arct. Eng. 122*(2), 118–124.

Nakaguchi, H., K. Hashimoto, & S. Muto (1968). An experimental study on aerodynamic drag of rectangular cylinders. *J. Jpn. Soc. Aeronaut. Space Sci. 16*, 1–5.

Ringwood, J., F. Ferri, N. Tom, K. Ruehl, N. Faedo, G. Bacelli, Y.-H. Yu, & R. G. Coe (2019). The Wave Energy Converter Control Competition: Overview. In *Proc. ASME 2019 38 Int. Conf. Ocean Offshore Arctic Eng. Vol. 10: Ocean Renew. En.*

SDIS (2024). *Simcenter STAR-CCM+ Documentation Version 2406*. Siemens Digital Industries Software. Unpublished work - available through Siemens.

Tian, X., L. Tao, X. Li, & J. Yang (2016). Hydrodynamic Coefficients of Oscillating Flat Plates at $0.15 \leq KC \leq 3.15$. *J. Mar. Sci. Tech. 22*, 101–113.